JATIS Journal of Astronomical Telescopes, Instruments, and Systems

RESEARCH PAPER

Development of the focal-plane CMOS detector for the GEO-X mission

Hiroshi Nakajima,[a,b,*] Shotaro Nakamura,[a] Koichi Hagino,[a] Ayumi Kiuchi,[a] Takuya Matsumoto,[a] Tohya Yamagami,[a] Tomokage Yoneyama,[b] Junko S. Hiraga,[c] Yuichiro Ezoe,[d] Masaki Numazawa,[d] Kumi Ishikawa,[d] and Hisashi Kitamura[e]

[a]Kanto Gakuinn University, College of Science and Engineering, Yokohama, Japan
[b]Japan Aerospace Exploration Agency, Institute of Space and Astronautical Science, Sagamihara, Japan
[c]Gakuin University, Department of Physics, Hyogo, Japan
[d]Tokyo Metropolitan University, Department of Physics, Hachioji, Japan
[e]National Institutes for Quantum Science and Technology, Chiba, Japan

ABSTRACT. We report a development status of a focal plane detector for the GEO-X (GEOspace X-ray imager) mission that will perform soft X-ray (≤ 2 keV) imaging spectroscopy of Earth's magnetosphere from a micro satellite. The mission instrument consists of a microelectromechanical systems (MEMS) X-ray mirror and a focal plane detector. A sensor with fine positional resolution and moderate energy resolution in the energy band of 0.3 to 2 keV is required. Because the observing target is the magnetosphere around the day-side Earth, the visible-light background must be decreased by shortening the integration time for readout. To satisfy the above requirements, a high-speed X-ray CMOS sensor is being evaluated as a primary candidate for the detector. Irradiating the flight candidate sensor with monochromatic X-rays, we obtained the energy resolution of 205 eV (FWHM) at 6 keV by cooling the devices to −15°C. Radiation tolerance of the sensor, especially in terms of total dose effect, is investigated with 100 MeV proton. The amount of degradation of energy resolution is < 50 eV up to 10 krad, which ensures that we will be able to track and calibrate the change of the line width in orbit.

 [DOI: 10.1117/1.JATIS.10.1.016001]

Keywords: X-rays; complementary MOS; micro satellite; photon counting

Paper 23039G received Mar. 31, 2023; revised Dec. 8, 2023; accepted Dec. 11, 2023; published Dec. 28, 2023.

1 Introduction

The Earth's magnetosphere that distributes in the height range of 10^3 to 10^5 km from the ground acts as a shield against the high-speed particles in the solar wind. Collision between charged particles in the solar wind (e.g., carbon, oxygen, neon, etc.) and neutral exospheric atoms, such as hydrogen, induce the charge exchange process and emit a photon at extreme ultraviolet or soft X-rays (Solar Wind Charge eXchange; SWCX).[1] The discovery of SWCX emission by XMM-Newton (e.g., Refs. 2–4) and Suzaku (e.g., Refs. 5–8) has stimulated research of the Earth's magnetosphere. The GEO-X (GEOspace X-ray imager) mission[9] aims to visualize SWCX for the first time by observing the emission from the highly elliptical orbit (HEO) with its apogee of 40 to 60 R_E (the radius of the Earth). Simulations performed in Refs. 1, 10–12 have demonstrated that the SWCX emission is sufficiently bright to image the cusps and magnetosheath regions.

*Address all correspondence to Hiroshi Nakajima, hiroshi@kanto-gakuin.ac.jp

There are several other missions that aim at imaging the Earth's magnetosphere.; SMILE, a joint mission between ESA and CAS, is planned to be launched in late 2024 or early 2025. It carries an X-ray and UV imager as well as *in-situ* measuring instruments, such as an ion analyzer and a magnetometer. The orbit will be a highly inclined elliptical one with an apogee of about $20\,R_E$. Another approved mission, LEXI, will observe SWCX emission from the surface of the Moon over multiple days in 2024.[13] The STORM[14] mission has been proposed to image the magnetosphere from a circular $30\,R_E$ orbit inclined 90 deg to the ecliptic. LSXI, another proposed Chinese mission,[15] will set an instrument on the Moon. On the other hand, GEO-X will obtain a bird's-eye view of the magnetosphere from low inclined orbit (<30 deg), so the emitting regions can be clearly identified. Furthermore, the topology of the magnetosphere dynamically varies by the solar flare and coronal mass ejection with the timescales of minutes and hours. GEO-X will capture the variation of structures in response to solar activities.

As a scientific instrument, we develop an ultralightweight telescope consisting of a MEMS (microelectromechanical systems) X-ray telescope[16,17] and compact focal plane detector with an optical blocking filter. We employ a new X-ray imaging spectrometer utilizing a scientific complementary MOS (CMOS) sensor.[18] Recently the CMOS sensor has been improved in terms of noise performance. Typically, it has readout noise and dark current of a few electrons per second and per pixel even at room temperature, which makes it unable to operate in photon counting mode in the soft X-ray range. Several applications have been already realized in the rocket experiment, FOXSI3,[19,20] which observes solar X-rays. An X-ray wide-field survey mission, Einstein Probe,[21,22] and an X-ray timing and polarimetry mission, eXTP,[23] also carry CMOS sensors. Recently, polarimetric performance has been verified,[24] and a future mission is being established.[25] These applications have verified that CMOS sensors have moderate energy resolution and energy range with a relatively higher temperature compared with those of conventional CCD cameras. Furthermore, the high-speed readout performance brings a low visible-light background level, which is essential for observing the day-side Earth.

In this paper, we employ two backside illumination type CMOS sensors that are originally designed for visible light/UV imaging to measure its X-ray spectroscopic performance. Specifications of the devices and their evaluation results are described in Sec. 2 and Secs. 3 and 4, respectively, followed by a summary in Sec. 5.

2 Flight Candidate Sensors

A candidate of the focal place sensor is a backside-illumination type GSENSE 400 device fabricated by Gpixel Inc.[26] It has a 4 Mpixels format with a standard 4T pixel architecture.[27] The specifications of the devices used in this work are summarized in Table 1. Both sensors are originally developed as sensitive imaging sensors in visible light (TVISB type) and ultraviolet (UV type). The picture of both sensors is shown in Fig. 1. The advantages of the sensor are low readout noise and dark current, which are essential items for soft X-ray spectroscopy. The large fullwell capacity (91 ke^- for 400BSI-TVISB) enables us to cover a wide energy range of X-rays. The operating temperature in the initial evaluation test is set to be −15°C. The device is mounted to zero insertion force sockets in a printed circuit board (PCB), and the glass lid is always removed in the test. The PCB and a part of wire harness are also cooled as a whole. The exposure time is set to be 0.4 s throughout the initial test because it is suitable for evaluating dark current

Table 1 Specifications of the sensors used in this work.

Device name	400BSI-UV	400BSI-TVISB
Pixel size	11 μm × 11 μm	
Number of effective pixels	2048 × 2048	
Readout noise (e-rms)	1.6	
Dark current (e-/pix/s)	<0.5 @ −16°C	<0.68 @ −15°C

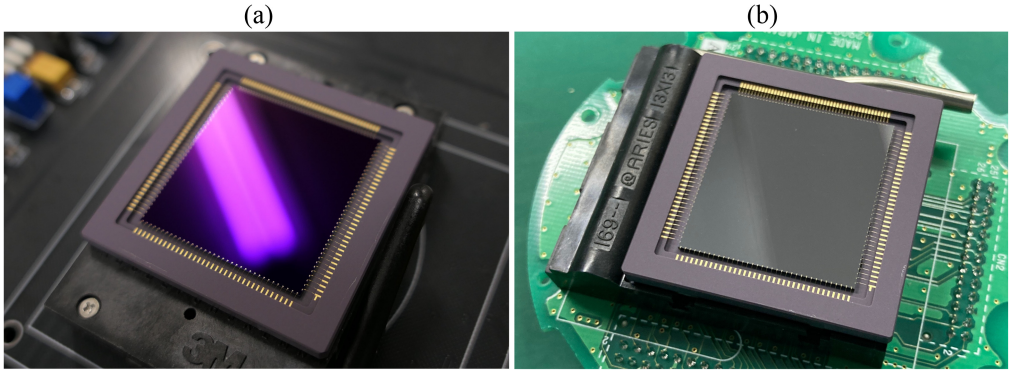

Fig. 1 CMOS sensors adopted for the GEO-X mission, which has a 4 Mpixels format with a standard 4T pixel architecture. (a) TVISB type and (b) UV type are evaluated.

shot noise. The dynamic range is set to be 12-bit in this work. A rolling shutter is adopted because of its low noise characteristic.

The whole arrays of both sensors are irradiated with monochromatic X-rays from the radioisotope ^{55}Fe source as an initial test to evaluate the X-ray spectroscopic performance. The exposure time, driving voltage, and sequence of the readout are set to be common between the sensors. Because signal charges produced as a result of photoelectric absorption distribute across the pixel boundary with a certain probability, X-ray events are classified as single-pixel events and multi-pixel events. We arrange two threshold values for the classification. First, if a pulse height of a pixel exceeds the "event threshold" and the pulse height is higher than any of the surrounding eight pixels, we regard the pixel as the event center. Next, the pulse height of the surrounding pixels is examined. If at least one of them exceeds the "split threshold," then the events are classified as multi-pixel events, whereas a single-pixel event has no surrounding pixels that exceed the threshold.

The monochromatic X-ray spectra are shown in Fig. 2. The spectra are extracted from the entire region of the sensors. The UV sensor exhibits a similar line spread function between single- and multi-pixel events, which enables us to resolve Mn Kα and Kβ lines in the summed spectrum. The energy resolution of single pixel events is 204.6 ± 2.4 eV [full width at half maximum (FWHM)]. This is comparable performance to that of the conventional CCDs that are cooled to ~ -100°C. Another note is that the lower limit of the energy band for the UV sensor is ~0.2 keV, which satisfies the observation band of GEO-X (0.3 to 2.0 keV). On the other hand, the TVISB sensor shows that the pulse height of multi-pixel events is remarkably

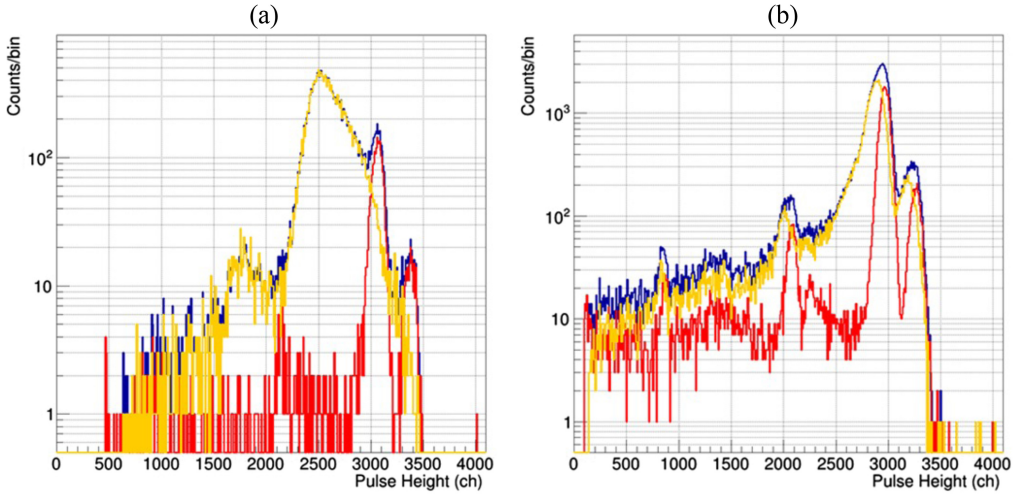

Fig. 2 Spectra obtained with (a) TVISB and (b) UV by irradiating the sensors with ^{55}Fe. Red, yellow, and blue data show the spectra extracted from a single pixel event, multi-pixel events, and the sum of them, respectively.

lower than that of single-pixel components, and the resolution of single-pixel events of 227.0 ± 1.9 eV (FWHM) is larger than that of the UV sensor. The number ratios of multi-pixel and single-pixel events are 0.317 ± 0.013 for the UV sensor and 0.100 ± 0.002 for the TVISB sensor. The former shows a relatively large ratio that leads to a better spectral performance than the latter.

In particular, the profile of the TVISB type sensor was reported in Ref. 28. The difference of the line profile between single- and multi-pixel events was seen in the other sensors of the same manufacturer.[23] Because analog-to-digital converters are implemented for each column in both sensors, the difference of the profile seen only for the TVISB sensor should not be due to the gain non-uniformity among columns. Furthermore, the disagreement of the peak pulse height is not peculiar to a specific readout system. Hence, it should be due to the recombination of the signal charge[29] inside the sensor when X-rays are absorbed in the non-depleted region.[30]

The two kinds of sensors are fundamentally fabricated from the same wafer, although the sensitivity in the specific wavelength is separately optimized by changing the treatment of the incident layer. Therefore, the specific resistance of the epitaxial layer must be almost the same value, and the difference in the spectrum is due to the thickness of the epitaxial layer. UV and TVISB sensors have an epitaxial layer with a thickness of 4 and 10 μm, respectively. It is indicated that the electric field in a part of the wafer of the TVISB sensor is not sufficiently strong, and hence the sensor is not fully depleted. When the X-rays are absorbed in the non-depleted layer, the signal charges get diffused across the pixel border before they are drifted and integrated in the pinned photodiode. This results in a low pulse height in the spectrum. Although it is worth optimizing the drive voltage of the TVISB sensor to investigate the charge loss issue, here we select the UV sensor as the primary candidate because the overall line spread function is simpler.

3 Radiation Tolerance

We plan to put the GEO-X into a HEO with a low inclination angle of <30 deg and an apogee of 40 to 60 R_E. The expected dose rate of the HEO is 10 krad/year, which is higher than that of the low-earth orbit because the satellite will pass the radiation belt. In general, radiation damage to the CMOS sensor is classified to total ionizing dose (TID) and single event effect (SEE). TID is primarily induced by the trapped protons and leads to two kinds of performance degradation. The buildup of trapped positive charge in the dielectrics, especially near the transfer gate (TG), has an influence on the charge transfer efficiency across TG. The buildup of the interface states at the Si/oxide interfaces results in an increase of dark current from low dose level. In addition, displacement damage collapses the lattice and produces a charge trap in the sensitive layer due to a total non-ionizing dose. SEEs are individual events that occur when an ionizing particle deposits energy that is large enough to disturb the performance of the sensor and/or electronics. Investigation results of the SEE tolerance of our devices will be reported in other paper.

We investigate the tolerance of the candidate chips against the TID effect by irradiating the bare chips with 100 MeV protons at a heavy ion medial accelerator in Chiba, Japan. Considering that our planned mission lifetime is a minimum of 1 year, we set the total fluence to be 20 krad/cm^2, which corresponds to 2.2×10^{11} p/cm^2. The device under test is kept in air pressure and room temperature throughout the test. We converge the proton beam and do not apply any scattering medium in front of the chip. The beam size and its position are set to be 2 mm $\times$ 3 mm at the center of the array. After the damage, the dark current increases around the beam center, as shown in Fig. 3(a). Assuming that the increase of the dark current is in proportion to the amount of dose at that position, we define the analysis region following the contour map as depicted in Fig. 3(b) and calculate the dose in each region. The total dose in the center region with the severest damage is over 100 krad, which corresponds to 10 years in HEO.

Figure 4 shows the spectrum extracted from regions 1 to 6. Multiple anomalously narrow lines can be seen only in the single event spectrum. Each line corresponds to a specific pixel that has an almost constant pulse height throughout the data acquisition. If the constant level exceeds the event threshold after the dark subtraction, it appears to be an abnormally narrow emission line. To eliminate these false events, a threshold of the frequency of the event appearance is introduced. If the frequency exceeds 1% of the frame number, the pixel is regarded as "hot" due to the radiation damage. The threshold needs to be tuned for onboard data processing

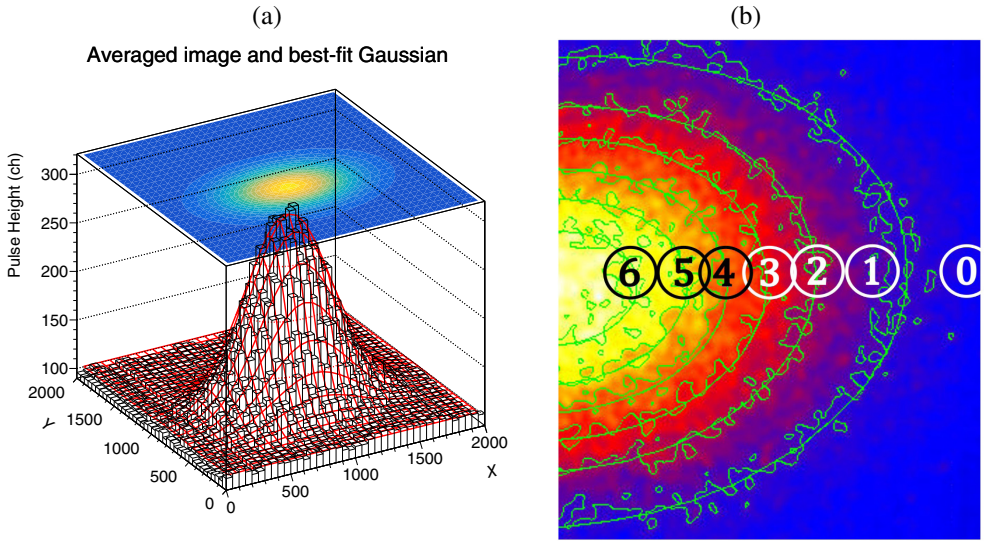

Fig. 3 (a) Dark frame image of 400BSI UV sensor showing the increase of the dark current after the radiation damage by protons. (b) Definition of the analyzed regions in the trimmed dark frame image. Borders of the regions are adopted from the contours that are drawn with six steps in linear scale from the bottom and top of the pulse height distribution.

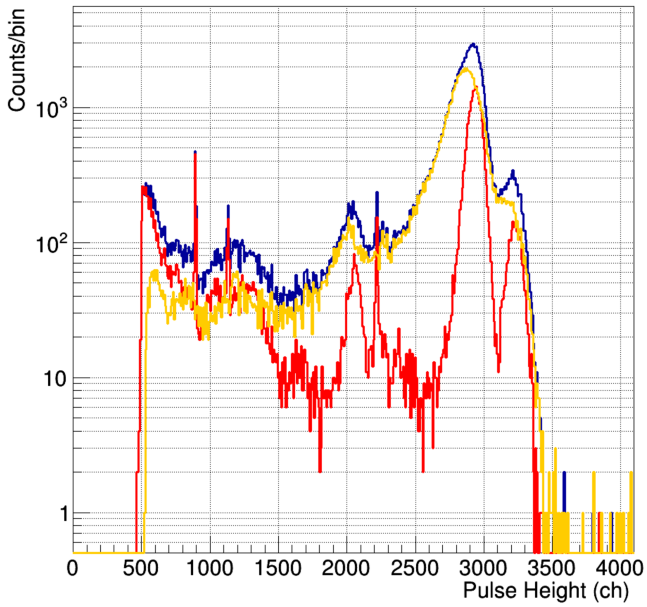

Fig. 4 ^{55}Fe spectrum extracted from the damaged region [regions 1 to 6 in Fig. 3(b)]. The meaning of the colors is the same as described for Fig. 2.

because the number of frames continuously obtained depends on the orbital phase, etc. The fraction of the hot pixels that is discriminated with above threshold is 2.5%. This would be compensated by observation with a longer duration than that initially planned.

The spectroscopic performance is affected by the increase of read-out noise (RON) and dark current. We evaluate both parameters using the frame data varying with the exposure time. The exposure time is set to be from 0.4 to 1.6 s/frame in steps of two. Figure 5 shows the dependence of the mean pulse height in each region defined in Fig. 3(b). The mean value and the exposure time are in the linear relation for every region. The slope of the best-fit linear function corresponds to the dark current in the region. The dispersion of the pulse height can be decomposed into the contribution by the RON and that by the dark current shot noise. The RON is derived with the assumption that the charge by the dark current has a normal distribution.

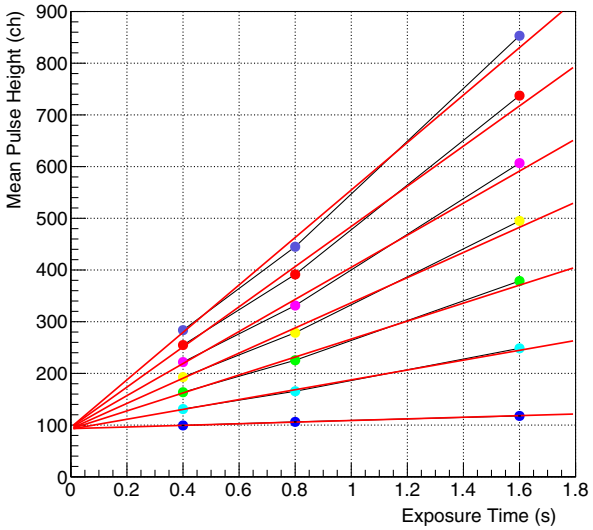

Fig. 5 Mean pulse height as a function of the exposure time measured for each region shown in Fig. 3(b). Blue, light blue, light green, yellow, magenta, orange, and purple correspond to region numbers zero to 6, respectively.

Figure 6 shows the RON and dark current as a function of the dose. Both parameters significantly increase after 3 krad.

The energy resolution is a rather practical parameter for verifying the spectroscopic performance of the sensor in orbit. Spectra from ^{55}Fe are extracted from each region, and the Mn Kα peaks are fitted with the Gaussian function for summed spectra. Figure 7 shows the FWHM value as a function of the total dose. Note that all single- and multi-pixel events are included in the spectra that are fitted. The amount of degradation of the energy resolution is less than 50 eV up to 10 krad, which ensures that we will be able to track and calibrate the change of the line width in orbit. Even in the center region where most intensive damage occurs, Mn Kα and Kβ are well resolved even in the center region that is severely damaged.

The increase of the RON and dark current affects the lower edge of the effective energy range. To determine the requirement for the lower edge, the line width and the line profile in the response functions need to be taken into account. To measure the line intensity precisely, the lower edge needs to be set so that the energy range securely includes the whole line. Hence, to detect the characteristic X-rays from SWCX emission, such as O6+ and O7+, the requirement of the lower energy range is set to be 0.3 keV throughout the mission. A possible reason for the spectroscopic performance degradation is the increase of the hot pixels. If the significant amount

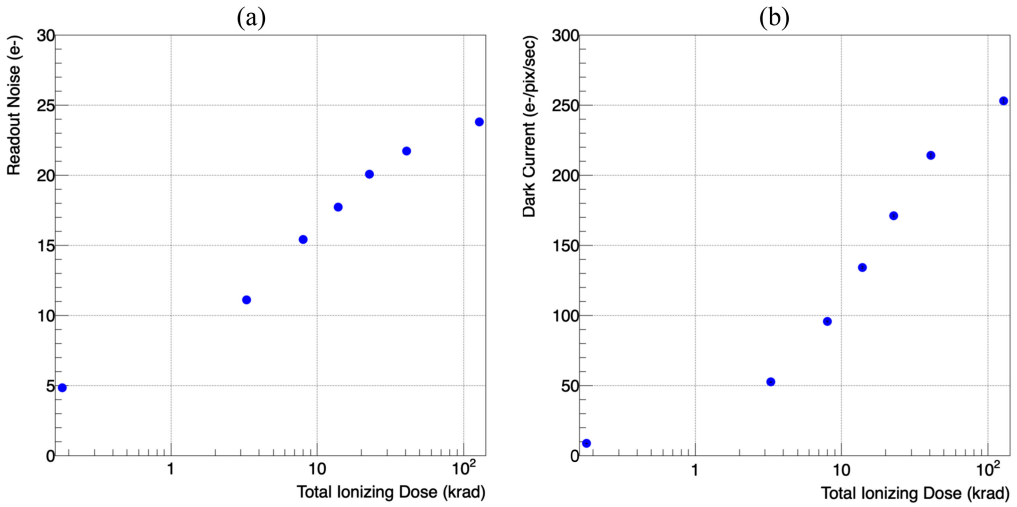

Fig. 6 (a) RON and (b) dark current as a function of the radiation damage.

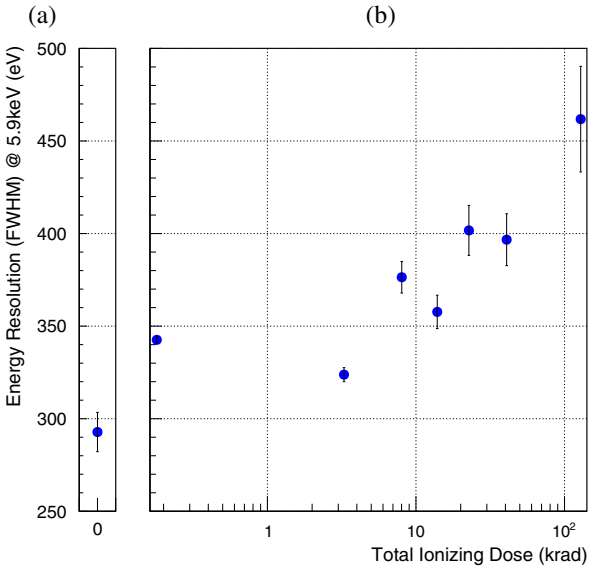

Fig. 7 Energy resolution as a function of TID. (a) A value obtained from data before the radiation damage test. (b) Data derived using the events extracted from regions in the damaged image [Fig. 3(b)].

of charge is produced in a pixel due to radiation damage and the amount is almost constant, the pixel is eliminated from the latter part of event processing. However, the frequency is too low to be regarded as hot pixels and the pulse height is around the event threshold (hereafter, we call this "less-hot pixels"), the spectrum is contaminated by the false events, especially around the lower edge. Similarly, when the pulse height by these false signal charges fluctuates around the split threshold and the position of the charges are just next to the genuine signal charges, they will be added to the original pulse height and will degrade the spectral resolution.

To minimize this effect, we grade each event according to the pulse height distribution around the event center pixel, as shown in Fig. 8. The basic method of this "grading" is conventionally adopted in the event processing of onboard X-ray CCDs. In the case of the CCD camera on board the Suzaku satellite, most of the X-ray events are considered not to split into a region larger than 2×2 pixels. Grade-7 events, in which the event spreads more than 2×2 pixels, are

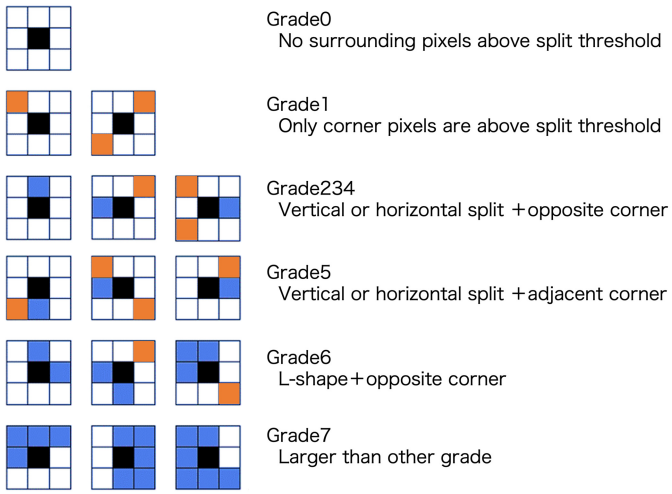

Fig. 8 Definition of event grading in the signal processing. Distributions of pixels for which pulse heights are larger than the split threshold as well as the `grade number are noted. The pixel designated with a black cell is the event center. Blue pixels are those with pulse heights above the split threshold and added to the total pulse height. Pixels colored with orange are also above the split threshold but not summed to the total pulse height.

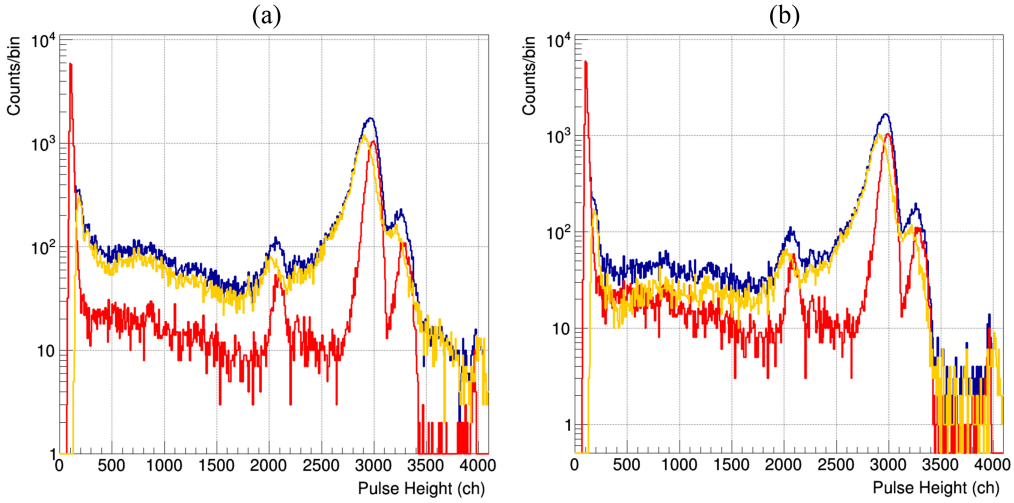

Fig. 9 ^{55}Fe spectrum (a) before applying the grading method and (b) after applying it. Note that yellow data in the grading method spectrum denote the events of Grades-2,3,4,6.

regarded as background events.[31] This criterion has been employed because charged particles induce elongated shapes of the charges along their tracks in the depletion layer, whereas X-ray photons generate a spheric or ellipsoidal charge distribution. Grade-1 and Grade-5 are considered not to be proper X-ray events because the signal distribution of this grade cannot be reproduced with an assumption of a single charge cloud. Instead, when multiple charge clouds are produced within a 3×3 pixel region in a frame cycle due to a pile-up or adjacent less-hot pixels, a part of such events can be categorized to these grades. Therefore, the grade method can be an effective process for eliminating possible less-hot pixels.

Then, the grade method is applied to the data obtained after the radiation dose as follows: Grades-0,2,3,4,6 are proper X-rays events and Grades-1,5,7 are recognized to be any of particle events, a pile-up of multiple X-ray events, or the events affected by less-hot pixels. The difference of the spectrum is shown in Fig. 9. The intensity of events just above the lower discrimination decreased, and the line profile of the multi-pixel events (Grade 2,3,4,6 events after applying grade method) has changed. In particular, lower discrimination is found to be < 0.3 keV, which satisfies the energy range requirement of the mission even after the radiation damage.

4 Linearity and Energy Resolution

To verify the effective energy range of GEO-X, it is essential to perform a imaging spectroscopy test in a vacuum environment. Then, we construct a dedicated test facility for investigation of the response function in the soft X-ray range utilizing an X-ray tube. The devices under test are irradiated with continuous X-rays as well as characteristic X-rays utilizing a secondary target. The voltage of the X-ray tube is set to be 10 kV. To investigate the response of the sensor against soft X-rays by eliminating the contribution of the dark current as far as possible, the sensor was cooled to -35°C in this test using Peltier cooler. An example of the spectrum is shown in Fig. 10. The spectrum exhibits numbers of lines that originate from the secondary target of glass (SiO_2), polymide tape with acryl paste, Ag target within the X-ray tube, and stainless steel, as noted in the figure. Multiple emission lines below 1.0 keV are O K, Fe L, and Si escape line of Cl Kα lines. They are resolved even in the multi-pixel events.

Assuming the incident X-ray energy of the lines, a linearity plot is derived as shown in Fig. 11(a). Several lines that are considered to be a mixture of multiple lines are eliminated from this plot. Deviation from the linear function is <5 ch, which corresponds to 10 eV in the soft X-ray range (<2.0 keV) and is sufficiently low considering the energy distribution of possible SWCX emission lines. The energy resolution as a function of the incident energy is plotted in Fig. 11(b). The data are fitted with a function of $\sqrt{aX + b}$. The data dispersion is large compared with the error for each data point, which is probably due to the mixing of multiple unidentified

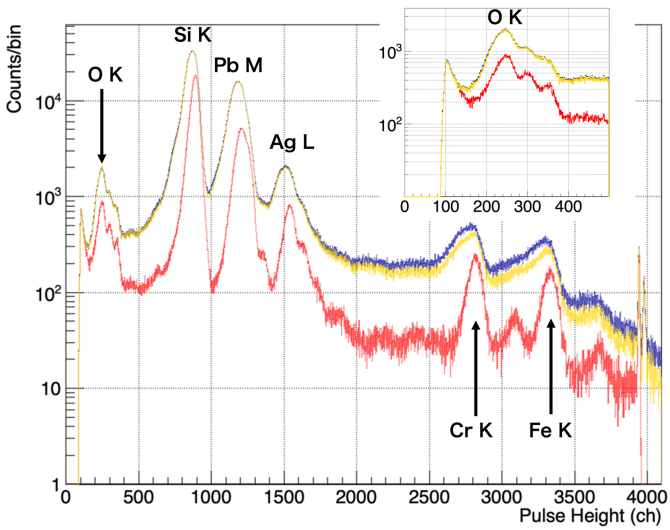

Fig. 10 Spectrum obtained utilizing Grade-2346X-ray tube (Ag target) and secondary target of SiO_2. The meaning of the colors is the same as described for Fig. 2. Inset is the close-up of the spectrum below 1 keV.

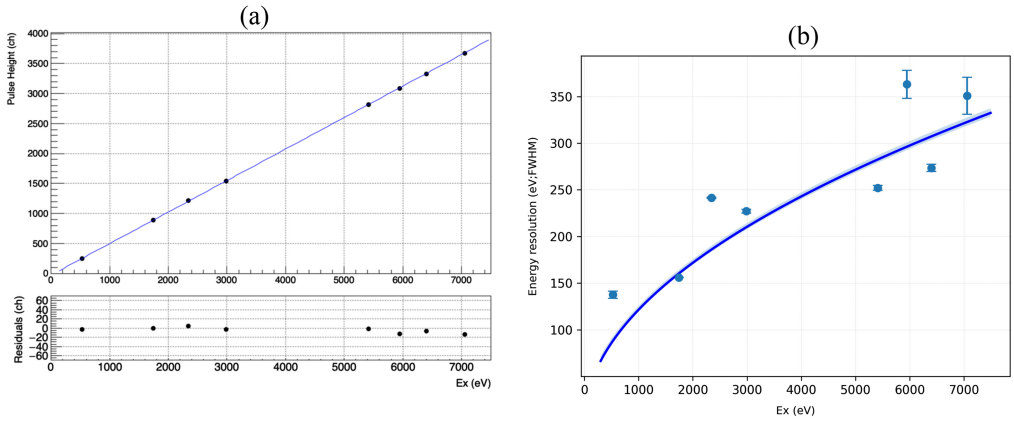

Fig. 11 (a) Linearity plot utilizing bright lines in the spectrum shown in Fig. 10. (b) Energy resolution as a function of the incident X-ray energy. Note that both data are measured from single-pixel events.

emission lines. The best fit model function indicates that the device satisfies the requirement of the energy resolution (120 eV at 0.6 keV).

5 Summary

The development status of the focal plane detector on board the GEO-X mission was reported. We adopt a back-side illuminated CMOS sensor that was originally developed for visible-light or ultraviolet imaging. GSENSE 400BSI UV was the primary candidate because we obtained a relatively better energy resolution of 205 eV (FWHM) at 6 keV by cooling the sensor to $-15\,^{\circ}$C before radiation damage and obtained a better line profile of the multi-pixel events. Radiation tolerance of the sensor was investigated with a 100 MeV proton. The degradation of energy resolution was < 50 eV up to 10 krad, which corresponds to the dose received during 1 year in the planned orbit. This result ensures that we will be able to track and calibrate the change of the line width throughout the mission. We also confirmed that multiple lines below 1 keV are resolved and energy resolutions are evaluated as well as linearity performance. The best fit model function indicates that the device satisfies the requirement of the energy resolution.

Code and Data Availability

The data that support the findings of this article are not publicly available due to privacy. They can be requested from the author at hiroshi@kanto-gakuin.ac.jp.

Acknowledgments

We acknowledge extensive support from Kanematsu Futuretech Solutions Corporation to test and evaluate the CMOS sensors. This work was supported by JSPS KAKENHI Grant Nos. JP21H04972, JP18H01256, JP20H00177, JP20KK0071.

References

1. I. P. Robertson et al., "X-ray emission from the terrestrial magnetosheath including the cusps," *J. Geophys. Res. Space Phys.* **111**(A12), A12105 (2006).
2. S. L. Snowden, M. R. Collier, and K. D. Kuntz, "XMM-Newton observation of solar wind charge exchange emission," *Astrophys. J.* **610**, 1182–1190 (2004).
3. S. L. Snowden et al., "Observation of solar wind charge exchange emission from exospheric material in and outside Earth's Magnetosheath 2008 September 25," *Astrophys. J.* **691**, 372–381 (2009).
4. J. A. Carter, S. Sembay, and A. M. Read, "Identifying xmm-newton observations affected by solar wind charge exchange - Part II," *Astron. Astrophys.* **527**, A115 (2011).
5. R. Fujimoto et al., "Evidence for solar-wind charge-exchange X-ray emission from the Earth's Magnetosheath," *Publ. Astron. Soc. Jpn.* **59**, S133–S140 (2007).
6. Y. Ezoe et al., "Time variability of the geocoronal solar-wind charge exchange in the direction of the celestial equator," *Publ. Astron. Soc. Jpn.* **62**, 981–986 (2010).
7. K. Ishikawa et al., "Suzaku observation of strong solar-wind charge-exchange emission from the terrestrial exosphere during a geomagnetic storm," *Publ. Astron. Soc. Jpn.* **65**, 63 (2013).
8. D. Ishi et al., "Suzaku detection of enigmatic geocoronal solar wind charge exchange event associated with coronal mass ejection," *Publ. Astron. Soc. Jpn.* **71**, 23 (2019).
9. Y. Ezoe et al., "GEO-X (GEOspace X-ray imager)," *Proc. SPIE* **12181**, 1218124 (2022).
10. I. P. Robertson and T. E. Cravens, "Spatial maps of heliospheric and geocoronal X-ray intensities due to the charge exchange of the solar wind with neutrals," *J. Geophys. Res. Space Phys.* **108**(A10), 8031 (2003).
11. D. G. Sibeck, "Imaging plasma density structures in the soft X-rays generated by solar wind charge exchange with neutrals," *Space Sci. Rev.* **214**, 79 (2018).
12. Y. Matsumoto and Y. Miyoshi, "Soft X-ray imaging of magnetopause reconnection outflows under low plasma-β solar wind conditions," *Geophys. Res. Lett.* **49**(19), e2022GL101037 (2022).
13. U. Paw et al., "X-ray micropore optic array preliminary calibration results for the lunar environment heliospheric X-ray imager," *Proc. SPIE* **12181**, 121814N (2022).
14. D. G. Sibeck et al., "Quantifying the global solar wind-magnetosphere interaction with the solar-terrestrial observer for the response of the magnetosphere (STORM) mission concept," *Front. Astron. Space Sci.* **10**, 1138616 (2023).
15. Y. Guo et al., "A lunar-based soft X-ray imager (LSXI) for the earth's magnetosphere," *Sci. China Earth Sci.* **64**(7), 1026–1035 (2021).
16. Y. Ezoe et al., "Micropore X-ray optics using anisotropic wet etching of (110) silicon wafers," *Appl. Opt.* **45**, 8932–8938 (2006).
17. M. Numazawa et al., "First demonstration of X-ray mirrors using focused ion beam," *Jpn. J. Appl. Phys.* **55**, 06GP11 (2016).
18. H. Nakajima et al., "Development of the focal-plane CMOS detector for the GEO-X mission," *Proc. SPIE* **12181**, 121812C (2022).
19. S. Ishikawa et al., "High-speed X-ray imaging spectroscopy system with Zynq SoC for solar observations," *Nucl. Instrum. Methods Phys. Res., Sect. A* **912**, 191–194 (2018).
20. N. Narukage et al., "High-speed back-illuminated CMOS sensor for photon-counting-type imaging-spectroscopy in the soft X-ray range," *Nucl. Instrum. Methods Phys. Res. A* **950**, 162974 (2020).
21. W. Wang et al., "Developments of scientific CMOS as focal plane detector for Einstein Probe mission," *Proc. SPIE* **10699**, 106995O (2018).
22. Y. Chen et al., "Status of the follow-up X-ray telescope onboard the Einstein Probe satellite," *Proc. SPIE* **11444**, 114445B (2020).
23. C. Chen et al., "Performance of a focal plane detector for soft X-ray imaging spectroscopy based on back-illuminated sCMOS," *Nucl. Instrum. Methods Phys. Res., Sect. A* **1030**, 166465 (2022).

24. K. Asakura et al., "Sub-arcsecond X-ray imaging with multi-image X-ray interferometer module (MIXIM): introduction of a periodic coded-aperture mask," *Proc. SPIE* **12181**, 1218129 (2022).
25. K. Hayashida et al., "Sub-arcsecond imaging with multi-image X-ray interferometer module (MIXIM) for very small satellite," *Proc. SPIE* **10699**, 106990U (2018).
26. C. Ma et al., "A 4MP high-dynamic-range, low-noise CMOS image sensor," *Proc. SPIE* **9403**, 940305 (2015).
27. E. R. Fossum, "CMOS image sensors: electronic camera-on-a-chip," *IEEE Trans. Electron Devices* **44**, 1689–1698 (1997).
28. N. Ogino et al., "Performance verification of next-generation Si CMOS soft X-ray detector for space applications," *Nucl. Instrum. Methods Phys. Res., Sect. A* **987**, 164843 (2021).
29. D. Schroder, "Carrier lifetimes in silicon," *IEEE Trans. Electron Devices* **44**(1), 160–170 (1997).
30. M. S. Haro et al., "Soft x-rays spectroscopy with a commercial CMOS image sensor at room temperature," *Radiat. Phys. Chem.* **167**, 108354 (2020).
31. K. Koyama et al., "X-ray imaging spectrometer (XIS) on board Suzaku," *Publ. Astron. Soc. Jpn.* **59**, S23–S33 (2007).

Hiroshi Nakajima is an associate professor in the College of Science and Engineering, Kanto Gakuin University in Kanagawa, Japan. He received his PhD from Kyoto University and performed post-doctoral research at Osaka University before joining Kanto Gakuin. His imaging spectroscopy experience includes development of CCD detectors onboard Suzaku, ASTRO-H, and XRISM satellite as well as front-end ASICs for X-ray imagers. He has over 60 refereed publications, which split between instrumentation papers and X-ray astronomical research.

Biographies of the other authors are not available.